

Personalized multiscale modeling of coronary plaque progression: the interaction between low-density-lipoprotein transport and cellular dynamics

Original

Personalized multiscale modeling of coronary plaque progression: the interaction between low-density-lipoprotein transport and cellular dynamics / Corti, Anna; De Nisco, Giuseppe; Wentzel, Jolanda J.; Migliavacca, Francesco; Morbiducci, Umberto; Chiastra, Claudio. - In: COMPUTER METHODS IN APPLIED MECHANICS AND ENGINEERING. - ISSN 0045-7825. - 448, Part A:(2026). [10.1016/j.cma.2025.118427]

Availability:

This version is available at: 11583/3006310 since: 2026-01-07T15:35:38Z

Publisher:

Elsevier

Published

DOI:10.1016/j.cma.2025.118427

Terms of use:

This article is made available under terms and conditions as specified in the corresponding bibliographic description in the repository

Publisher copyright

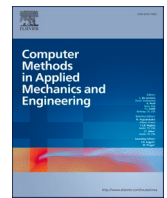
(Article begins on next page)



ELSEVIER

Contents lists available at [ScienceDirect](https://www.sciencedirect.com)

Computer Methods in Applied Mechanics and Engineering

journal homepage: www.elsevier.com/locate/cma

Personalized multiscale modeling of coronary plaque progression: the interaction between low-density-lipoprotein transport and cellular dynamics

Anna Corti^{a,*}, Giuseppe De Nisco^b, Jolanda J. Wentzel^d,
 Francesco Migliavacca^c, Umberto Morbiducci^b, Claudio Chiastra^b

^a Department of Electronics, Information and Bioengineering, Politecnico di Milano, Milan, Italy

^b Polito^{BIO}Med Lab, Department of Mechanical and Aerospace Engineering, Politecnico di Torino, Turin, Italy

^c Laboratory of Biological Structure Mechanics (LaBS), Department of Chemistry, Materials and Chemical Engineering "Giulio Natta", Politecnico di Milano, Milan, Italy

^d Department of Cardiology, Biomedical Engineering, Erasmus MC, Rotterdam, the Netherlands

ARTICLE INFO

Keywords:

Agent-based model (ABM)
 Three-pore model
 Coronary artery
 Atherosclerotic plaque

ABSTRACT

Multiscale agent-based modeling has shown promise in elucidating the mechanobiological mechanisms underlying atherosclerotic plaque formation and progression. However, the integration of advanced models of low-density lipoprotein (LDL) transport in the lumen and across the endothelium with agent-based models (ABMs) of plaque growth remains underexplored. Furthermore, patient-specific applications are lacking.

This study introduces a novel agent-based modeling framework for atherosclerosis, integrating hemodynamics and LDL transport in the lumen through computational fluid dynamics simulations, a three-pore model of trans-endothelial LDL migration, and an ABM of lipid and cellular dynamics. For the first time, the framework was applied to a patient-specific coronary artery and validated against 1-year follow-up data. Furthermore, it was used to explore potential plaque evolution over 5 years and under elevated LDL concentration.

The calibrated model predicted the 1-year variation in wall area in two patient-specific coronary cross-sections with an error of less than 10%. Simulated scenarios indicated that variations in blood LDL concentrations can result in distinct plaque morphologies, from localized to diffuse patterns.

This study provided an innovative, advanced multiscale model of atherosclerotic plaque formation and progression. As the first patient-specific application of a multiscale agent-based modeling framework for atherosclerosis with initial validation, this study underscored the potential of the approach for deciphering the mechanobiological pathways driving coronary plaque progression. The developed model provided valuable insights into how the interplay between LDL transport and hemodynamics influences arterial wall cellular dynamics in a patient-specific context.

* Corresponding author at: Anna Corti, PhD. Department of Electronics, Information and Bioengineering, Politecnico di Milano, Via Ponzio 34/5, 20133 Milan, Italy.

E-mail address: anna.corti@polimi.it (A. Corti).

<https://doi.org/10.1016/j.cma.2025.118427>

Received 14 March 2025; Received in revised form 30 July 2025; Accepted 19 September 2025

Available online 30 September 2025

0045-7825/© 2025 The Author(s). Published by Elsevier B.V. This is an open access article under the CC BY license (<http://creativecommons.org/licenses/by/4.0/>).

1. Introduction

With approximately 8.9 million deaths annually worldwide, coronary artery disease (CAD) is the leading cause of vascular disease-related morbidity and mortality [1]. CAD is primarily caused by atherosclerosis, a chronic inflammatory disease that leads to the accumulation of fatty plaques in the arterial walls, narrowing the vessel lumen [2]. Atherosclerotic arterial remodeling occurs in two consecutive phases, known as Glagov's phenomenon [3,4]: (i) initial outward compensatory enlargement, which maintains the lumen size despite plaque formation, and (ii) lumen narrowing, which begins when the plaque occupies 30-40% of the area enclosed by the internal elastic lamina [3]. Among the various biological, systemic, and biomechanical factors that influence the initiation and progression of atherosclerosis, elevated plasma levels of low-density lipoproteins (LDL) are considered the primary driver of lesion development [2,5]. LDL infiltration and subsequent lipid accumulation in the arterial intima are hallmarks of early atherosclerosis [2, 6]. Animal and human studies suggest that atherosclerotic lesions commonly develop in regions where high LDL concentrations co-localize with near-wall flow disturbances, particularly low and disturbed wall shear stress (WSS) [7]. Hemodynamic disturbances impair endothelial function, increasing LDL uptake by the arterial wall and promoting atherogenesis [7-9].

Computational models have been proposed to study the critical role of LDL transport in both idealized and patient-specific arteries, including coronary [10], carotid [11], femoral arteries [12], and the aorta [13]. While these studies have contributed to elucidating some of the mechanistic links between disturbed hemodynamics and LDL intimal infiltration, most have overlooked arterial wall remodeling resulting from plaque growth [14]. Only a few studies have incorporated plaque growth into fluid-wall mass transfer models [12,15-21], providing a more accurate representation of the pathological process. These studies modeled the arterial wall as a continuum, using sets of partial differential equations to describe the dynamics of atherogenic species (e.g., LDL, inflammatory cells, cytokines, arterial cells). In contrast, multiscale agent-based modeling frameworks offer a more detailed representation of biological systems by incorporating morphological features, tissue heterogeneity, and the intrinsic randomness of biological phenomena [22]. However, the integration of LDL transport models in the lumen and across the endothelium with agent-based models (ABMs) of plaque growth remains underexplored [23], and patient-specific applications are lacking. In this context, the present study introduces a novel multiscale model that couples numerical simulations of hemodynamics and LDL transport with an ABM of arterial cellular dynamics. This approach enables the simulation of mechanobiological processes underlying atherosclerotic plaque initiation and progression in a patient-specific coronary artery. Building on a previous investigation [24], this study introduces several methodological

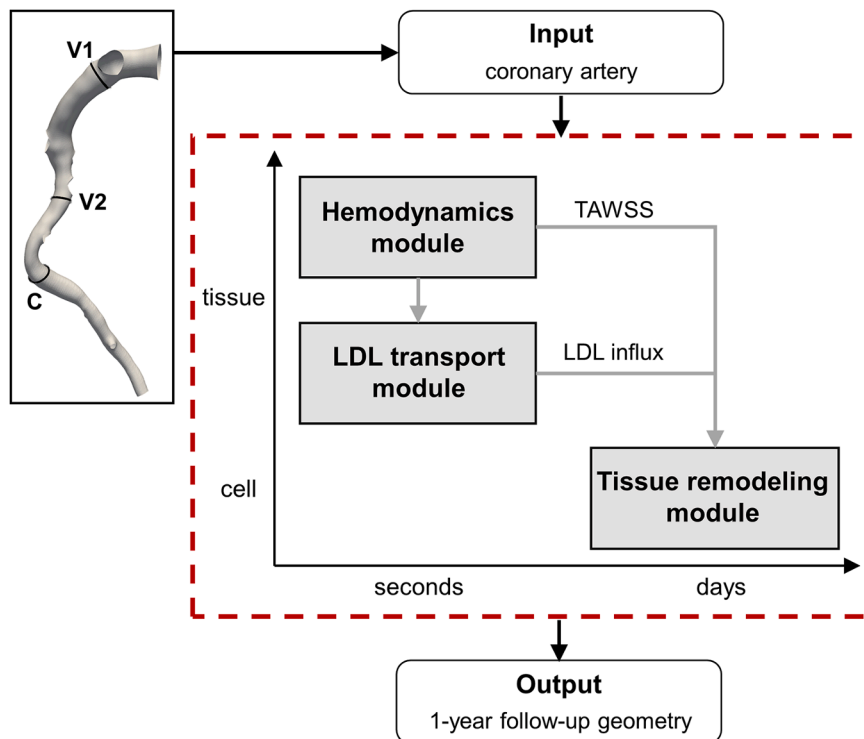


Fig. 1. Multiscale computational framework. Starting from the coronary artery model, the framework (dashed red box) simulates plaque formation and progression over 1 year in a patient-specific left anterior descending coronary artery. The framework consists of three modules: (i) the hemodynamics module at the tissue-second scale, computing the time-average wall shear stress (TAWSS) through transient computational fluid dynamics simulation, (ii) the low-density-lipoprotein (LDL) transport module at the tissue-second scale, computing the LDL trans-endothelial influx by combining a wall-free model and a three-pore model, and (iii) the tissue remodeling module at the cell-days scale, in which a bidimensional (2D) agent-based model (ABM) simulates plaque formation and progression in response to the TAWSS and the LDL influx, in three selected cross-sections (C, V1 and V2).

advancements, integrating hemodynamics, LDL transport and agent-based modeling to simulate plaque growth and arterial wall remodeling. Furthermore, the proposed framework has been extended to patient-specific applications, including ABM calibration and model validation. Specifically, the present work introduces the following key methodological improvements over the previous study [24]: (i) transient computational fluid dynamics (CFD) simulations of blood flow, replacing the earlier steady-state approach; (ii) numerical simulation of LDL mass transport in the bloodstream, achieved by coupling CFD with advection-diffusion equations; (iii) a three-pore model of the endothelium that bridges the continuum description of LDL transport in the lumen with agent-based modeling of LDL infiltration into the arterial wall; (iv) an enhanced model of plaque growth that incorporates Glagov's phenomenon to account for both compensatory enlargement and luminal narrowing; (v) refinements to agent activities, including the adoption of an optimized WSS-based input function—previously proposed and calibrated in our recent in-stent restenosis studies [25,26]—and the introduction of a lipid-induced inflammatory trigger influencing smooth muscle cell (SMC) and extracellular matrix (ECM) dynamics.

2. Methods

2.1. Multiscale framework

Fig. 1 illustrates the multiscale framework for atherosclerosis, adapted from a previous study by the research group [24], to incorporate (i) the effect of LDL concentration polarization at the lumen surface, computed via numerical simulation, (ii) LDL intimal infiltration, modeled using the three-pore theory to bridge the continuum-based description of LDL transport in the lumen with the agent-based LDL infiltration in the arterial wall, and (iii) Glagov's phenomenon for arterial remodeling. Briefly, the framework takes a 3D model of a coronary artery at baseline (T0) as input and it simulates hemodynamic- and LDL-driven plaque formation to generate the vessel geometry at 1-year follow-up (T1) as output. The framework integrates three key modules: (i) the hemodynamics module, which computes the WSS profile via CFD simulation, (ii) the LDL transport module, which includes a wall-free transport model to compute LDL polarization at the lumen surface and an adapted three-pore formulation to determine trans-endothelial LDL influx, and (iii) the tissue remodeling module, which uses a 2D ABM to simulate LDL intimal accumulation and the perturbed activity of intimal SMC and ECM in regions with low WSS and high LDL concentrations at the lumen surface.

The framework was applied to a patient-specific diseased left anterior descending (LAD) coronary artery, with an inlet lumen diameter of 6 mm, an outlet lumen diameter of 2.4 mm, and a length of 84 mm (Fig. 1) [27,28]. The LAD artery was imaged at T0 using computed coronary tomography angiography (CCTA) and intravascular ultrasound (IVUS), and at T1 by IVUS alone, as detailed in [28, 29]. The IVUS-derived variation in wall area (T1-T0) along the vessel centerline [27] was used to calibrate and validate the modeling framework at three selected cross-sections—the only regions that showed measurable arterial wall growth over 1 year of follow-up. Among them, one cross-section (C) was randomly selected for calibration, while the remaining two (V1 and V2) were used for validation (Fig. 1).

2.1.1. Hemodynamics module

The 3D LAD geometry was reconstructed by combining CCTA and IVUS data as described elsewhere [30], and discretized using tetrahedral elements in the lumen and 30 layers of high-quality prismatic elements in the near-wall region, employing Fluent Meshing (Ansys Inc., Canonsburg, PA, USA) [13]. The Supplementary Materials provides further details on the boundary layer dimensions. Transient simulations of blood flow were performed using a finite volume code (Fluent, Ansys Inc.) with previously adopted CFD settings [27]. Blood was modeled as a homogeneous, incompressible Newtonian fluid with a constant density of 1060 kg/m³ and a dynamic viscosity of 0.0035 Pa·s [31]. A no-slip condition was applied at the arterial wall. In vivo ComboWire Doppler velocity measurements were used to derive the patient-specific inlet and outlet fluid dynamic boundary conditions [27]. Specifically, a parabolic time-dependent velocity profile was prescribed at the inlet, based on the most proximal Doppler velocity measurement. Flow-split was applied at the outlets, considering the difference between upstream and downstream Doppler velocity-based flow rate measurements. Details on the numerical schemes and convergence criteria are provided in the Supplementary Materials.

The simulation was run until the maximum local percentage difference in time-averaged WSS magnitude (TAWSS) between two consecutive cardiac cycles was less than 1%. At the end of the CFD simulation, the TAWSS profiles at the cross-sections C, V1 and V2 were extracted for the ABM analysis.

2.1.2. LDL transport module

To simulate LDL transport within the lumen compartment, a wall-free model solving the advection-diffusion equation for LDL in flowing blood was employed. The CFD mesh detailed above was used and the LDL transport simulation was carried in ANSYS Fluent on top of the converged blood flow CFD simulation. LDL was assumed to be dissolved in the blood and treated as a passive, non-reacting scalar [27]. The following boundary conditions were imposed [13,27]: a uniform concentration profile at the inlet, set to the average value observed in the population that includes the investigated subject [28] ($C_0 = 2.84$ mmol/L), a stress-free condition at the outlets, and a zero net LDL flux through the lumen surface, enforced via the mass conservation condition of Eq. 1:

$$c_{ls}v_{ls} - D_l \frac{\partial c_l}{\partial n} = 0, \forall \mathbf{x} \in \Gamma_{ls}, t > 0 \quad (1)$$

where c_l and c_{ls} are the LDL concentrations in the lumen and at the lumen surface Γ_{ls} , respectively, $D_l = 5.983 \cdot 10^{-12}$ m²s⁻¹ is LDL

diffusivity in flowing blood, $v_{ls} = 4 \cdot 10^{-8} \frac{m}{s}$ is the water filtration velocity at Γ_{ls} . A uniform initial LDL concentration (CO) was applied to both the fluid domain and the lumen surface. The simulation was carried out until the maximum local percentage difference in normalized LDL concentration between two consecutive simulated cardiac cycles dropped below 1%. At the end of the simulation, the normalized LDL concentration (c_{ls}/c_0) was extracted from the three cross-sections (C, V1, V2) for the ABM analysis.

To couple the wall-free transport model with the LDL influx in the ABM arterial wall, the three-pore model was adopted to represent the endothelium [Table 1] [32,33]. This model describes LDL transport through the endothelium via three mechanisms: the vesicular pathway (v), normal junctions (nj), and leaky junctions (lj), and embeds a WSS-dependent description of endothelial permeability. Specifically, the model was used to calculate the local LDL flux into the arterial wall J_s , which serves as one of the inputs for initializing the ABM.

2.1.3. Tissue remodeling module

The tissue remodeling module involved a 2D ABM simulation in the MATLAB environment (MathWorks, Natick, MA, USA). It was used to simulate the atherosclerotic plaque development and arterial wall remodeling in response to TAWSS and the solute flux (J_s) distributions. The general structure and working rules of the ABM are extensively detailed in previous studies [24,26,34]. Briefly, the ABM was implemented on a 350×350 hexagonal grid, with a scale factor of $37.5 \mu m$ per ABM site. The intima, media, and adventitia layers were defined using patient-specific lumen geometry, and circular internal elastic lamina, external elastic lamina, and outer border, along with layer thicknesses derived from literature [24,26]. Cells and ECM agents were distributed within the ABM according to layer-specific densities [24,35].

The ABM was initialized with inputs based on WSS and LDL ($WSSinput$ and $LDLinput$, respectively), which determined the probabilistic behavioral rules of lipid and cellular activities (Table 2). $WSSinput$ reflected the modulating effect of WSS on SMC dynamics, where increased synthetic and proliferative activities of SMCs occur in low WSS regions [36]. Specifically: (i) the TAWSS computed through the hemodynamic module was assigned to each lumen wall agent, (ii) a sigmoid function was applied to represent the inverse relationship between TAWSS and the hemodynamic triggering input (low TAWSS corresponds to a high input), and (iii) the input was propagated through the intima layer using a sinusoidal function (Table 2) [26]. $LDLinput$ was defined as a normalized form of J_s , calculated via the three-pore model, which depends on both the TAWSS and the LDL concentration at the lumen surface (C_l). To account for the inflammatory cascade triggered by lipid accumulation in the intima [37], an inflammatory state (I) was modeled in terms of a 2D Gaussian distribution, whose amplitude and intensity varied linearly with the lipid content in the intima (Table 2).

Probabilistic behavioral rules (Table 2) were defined to simulate LDL infiltration into the intima, cell mitosis/apoptosis, and ECM production/degradation, based on local levels of $WSSinput$, $LDLinput$ and I . Specifically, the probability of LDL infiltration (p_{lip}^h , the likelihood of a lumen wall site being an access point for LDL infiltration into the intima) increased in regions where $LDLinput$ and I was higher. Proliferative and synthetic cellular activities ($p_{division}^h$ and $P_{ECMproduction}^h$) were more pronounced in regions with higher $WSSinput$

Table 1
Three pore model equations.

| | |
|---|---|
| Mass flux through the endothelium | $J_s = P_{app} C_l$ |
| Total apparent permeability of the endothelium (P_{app}) | $P_{app} = P_v + P_{app,nj} + P_{app,lj}$ |
| Apparent permeability of the leaky junctions ($P_{app,lj}$) | $P_{app,lj} = P_{lj} Z_{lj} + J_{v,lj} (1 - \sigma_{r,lj})$ |
| | $P_{lj} = \frac{w^2}{3} \frac{4w\varnothing}{R_{cell}}$ |
| | $\sigma_{r,lj} = 1 - \left(1 - \frac{3}{2} \alpha_{lj}^2 + \frac{1}{2} \alpha_{lj}^3\right) \left(1 - \frac{1}{3} \alpha_{lj}^2\right)$ |
| | $Z_{lj} = Pe_{lj} / (e^{Pe_{lj}} - 1)$ |
| | $Pe_{lj} = [J_{v,lj} (1 - \sigma_{r,lj})] / P_{lj}$ |
| | $J_{v,lj} = L_{p,lj} \Delta p_{end}$ |
| | $L_{p,lj} = \frac{w^2}{3\mu_p l_{lj}} \frac{4w\varnothing}{R_{cell}}$ |
| | $\varnothing = \frac{\#LC \times \pi R_{cell}^2}{S_{unit}}$ |
| | $\#LC = 0.307 + 0.805 \cdot (\#MC)$ |
| | $\#MC = 0.003797e^{14SI}$ |
| | $SI = 0.380e^{-0.790TAWSS} + 0.225e^{-0.0437TAWSS}$ |

$P_v = 1.92 \times 10^{-11} m/s$ permeability of the vesicular pathway, $P_{app,nj} = 0$ apparent permeability of the normal junctions; $P_{app,lj}$ apparent permeability of the leaky junctions (lj); P_{lj} diffusive permeability; $\sigma_{r,lj}$ solvent-drag reflection coefficient; Z_{lj} fractional reduction factor in solute concentration gradient at the entrance of lj pore; $J_{v,lj}$ volume flux; $w = 20 \text{ nm}$ half-width of lj; $R_{cell} = 15 \mu m$ radius of endothelial cell; $\alpha_{lj} = \frac{a}{w}$ with $a = 11 \text{ nm}$ (radius of LDL); Pe_{lj} modified Péclet number; $L_{p,lj}$ hydraulic conductivity; $\Delta p_{end} = 2400 \text{ Pa}$ pressure difference through the endothelium; $l_{lj} = 2 \mu m$ length of lj; $\mu_p = 10^{-3} \text{ Pa s}$ plasma viscosity; $\#MC$ and $\#LC$ are the number of mitotic cells and leaky cells; $S_{unit} = 0.64 \text{ mm}^2$ periodic circular unit area; SI endothelial cells shape index; WSS (Pa) wall shear stress

Table 2
Agent-based model probability equations.

| | |
|----------------------------------|--|
| <i>WSSinput</i> | $D(\text{TAWSS})^i = -\frac{1}{1 + e^{J_i(\text{TAWSS}^i - L_2)}} + 1$ $\text{WSSinput}^h = \begin{cases} D(\text{TAWSS})^i & \text{lumen} \\ \sum_i D(\text{TAWSS})^i \times \text{Amp} \times \left(1 + \cos\left(\pi \frac{x}{\text{dist}}\right)\right) & \text{intima} \end{cases}$ |
| <i>LDLinput</i> | $\text{LDLinput}^i = \left(\frac{J_{s_i} - J_{s_{\text{physio}}}}{J_{s_{\text{patho}}} - J_{s_{\text{physio}}}}\right) \cdot \left(\frac{C_i - C_{\text{min}}}{C_{\text{max}} - C_{\text{min}}}\right)$ |
| <i>Inflammation</i> | $A_{\text{inf}} = \begin{cases} A_0 + \frac{A_m}{\text{lip}_{\text{sat}}} \cdot \text{nlip} & 1 \leq \text{nlip} \leq \text{lip}_{\text{sat}} \\ A_{\text{max}} & \text{nlip} \geq \text{lip}_{\text{sat}} \end{cases}$ $\text{Int}_{\text{inf}} = \begin{cases} \text{Int}_0 + \frac{\text{Int}_m}{\text{lip}_{\text{sat}}} \cdot \text{nlip} & 1 \leq \text{nlip} \leq \text{lip}_{\text{sat}} \\ \text{Int}_{\text{max}} & \text{nlip} \geq \text{lip}_{\text{sat}} \end{cases}$ |
| <i>Intima dynamics</i> | $P_{\text{division}}^h = \begin{cases} \alpha_1 + \alpha_2 \text{WSSinput}^h & \text{nlip} = 0 \\ \alpha_1 + \alpha_2 \text{WSSinput}^h + \alpha_3 I^h & \text{nlip} > 0 \end{cases}$ $P_{\text{apoptosis}}^h = \alpha_1$ $P_{\text{ECMproduction}}^h = \begin{cases} \alpha_4 + \alpha_5 \text{WSSinput}^h & \text{nlip} = 0 \\ \alpha_4 + \alpha_5 \text{WSSinput}^h + \alpha_6 I^h & \text{nlip} > 0 \end{cases}$ $P_{\text{ECMdegradation}}^h = \frac{\alpha_4}{\beta_{\text{int}}}$ |
| <i>Media/Adventitia dynamics</i> | $P_{\text{division}}^h = P_{\text{apoptosis}}^h = \alpha_1$ $P_{\text{ECMproduction}}^h = \beta_{\text{med/adv}} \cdot P_{\text{ECMdegradation}}^h = \alpha_4$ |
| <i>Lipid infiltration</i> | $P_{\text{lip}}^h = \begin{cases} \alpha_7 \text{LDLinput}^h & \text{nlip} = 0 \\ \alpha_7 \text{LDLinput}^h + \alpha_8 I^h & \text{nlip} > 0 \end{cases}$ |
| <i>Parameters</i> | $\alpha_1 = 0.01; \alpha_2 = [0, 0.2] \text{ TBC}; \alpha_3 = [0, 0.7] \text{ TBC}; \alpha_4 = 0.0025; \alpha_5 = \frac{\alpha_2}{4}$ $\alpha_6 = \frac{\alpha_3}{4}; \alpha_7 = [0, 0.5] \text{ TBC}; \alpha_8 = [0, 0.5] \text{ TBC}$ $\beta_{\text{int}} = 1.55; \beta_{\text{med/adv}} = 2.5$ |

$J_{s_{\text{physio}}} = \text{LDL}$ influx computed through the three-pore model by considering $\text{WSS}=1 \text{ Pa}$ and $\text{C0}=1.8 \text{ mmol/L}$; $J_{s_{\text{patho}}} = \text{LDL}$ influx computed through the three-pore model by considering $\text{WSS}=0.4 \text{ Pa}$ and $\text{C0}=5.2 \text{ mmol/L}$; $C_{\text{min}}=1.8 \text{ mmol/L}$; $C_{\text{max}}=5.2 \text{ mmol/L}$; P_{division}^h : probability of cell mitosis; $P_{\text{apoptosis}}^h$: probability of cell apoptosis; $P_{\text{ECMproduction}}^h$: probability of extracellular matrix (ECM) production; $P_{\text{ECMdegradation}}^h$: probability of ECM degradation; I : inflammatory input; $\alpha_1, \alpha_2, \alpha_3, \alpha_4, \alpha_5, \beta_{\text{med}}, \beta_{\text{adv}}$: parameters driving agent probabilities; TBC: To be calibrated.

and I . In the media and adventitia layers, or in the intima layer when no external stimuli were present, baseline activities were set to maintain a balance between cellular mitosis and apoptosis, as well as ECM production and degradation. Parameter values were defined according to previous studies [24,26]. Additionally, parameters $\alpha_2, \alpha_3, \alpha_7, \alpha_8$ (Table 2) were calibrated to match observed arterial wall area variation over one year, as described in Section 2.2. Finally, parameters α_5, α_6 were related to parameters α_2, α_3 to balance ECM production relative to cell proliferation in the media layer, given the higher baseline ECM content compared to cellular content. Further details on the definition of probabilistic rule definitions can be found in previous studies [24,25,34].

The ABM simulation involves executing LDL and cellular activities at each time step. For LDL infiltration, 25% of lumen wall sites with $P_{\text{lip}}^h > 0.0001$ was processed per time step. These sites were ranked in descending order based on their probability, and they were designated as access sites for LDL if their probability exceeded a randomly generated number. If so, LDL entered the intima and was placed at a randomly selected site within a maximum distance of 6 sites from the access site. Once in the intima, LDL was treated as a lipid agent (i.e., the chemical processes LDL undergoes within the intima were not modeled). An aggregation algorithm was applied to promote lipid clusters formation: isolated lipids or clusters smaller than three lipids were identified and relocated to the nearest larger lipid cluster within a defined distance.

Regarding cellular activities, each agent was initialized with a random time within its biological cycle T_{agent} ($T_{\text{cell}}=24 \text{ hours}$, $T_{\text{ECM}}=4 \text{ hours}$), which was updated at each time step to ensure desynchronization of cellular activities [26,38]. When agents reached the end of their biological cycle, they became potentially active, and their internal time was reset at the next time step. At each time step, potentially active agents were identified, and agent-specific events (i.e., cell mitosis/apoptosis or ECM production/degradation) were tested. An event occurred only if the agent-specific event probability exceeded a randomly generated threshold. If the event was cell mitosis or ECM production, a new agent was generated, if the event was cell apoptosis or ECM degradation, the agent was removed.

LDL infiltration, along with the generation/removal of cells/ECM within the arterial wall, drives the reorganization of surrounding agents. Arterial wall remodeling was simulated by implementing (i) Glagov's phenomenon in the intima, which involves a two-phase process — outward-oriented agent dynamics, followed by inward-oriented agent dynamics — and (ii) outward-oriented agent

dynamics in the media and adventitia layers. According to Glagov’s phenomenon, lumen narrowing began once the area occupied by the growing atherosclerotic lesion reached 30% of the internal elastic lamina area (IEL) [39]. Therefore, at each time step, the stenosis value ($stenosis_{GL}$) was calculated as follows [3]:

$$stenosis_{GL}(t) = \frac{A_{IEL}(t) - A_{IEL}(0)}{A_{IEL}(t)} \tag{2}$$

where A_{IEL} is the area of the IEL at time t and at the initial condition. Finally, smoothing algorithms were applied to maintain regular internal and external borders [25].

To account for ABM stochasticity, the simulation was repeated ten times, and the output minimizing the root mean square deviation of the lumen contour from the average was selected as the representative condition [24].

2.2. Agent-based model calibration and use-case scenarios

While the parameters used for the hemodynamics and LDL transport module were either derived from clinical measurements or from literature (as reported in Supplementary Table S1), the ABM parameters $\alpha_2, \alpha_3, \alpha_7, \alpha_8$ (Table 2) were calibrated by defining an optimization problem, as described in [25]. The goal was to: (i) minimize the difference between the simulated variation in wall area and the *in vivo* measurements, and (ii) maintain the physiological ECM/SMC ratio by imposing a final-to-initial ratio, $ECM/SMC_{ratio_int} \in [0.5, 1.5]$, based on the assumption that the relative arterial ECM/cell composition cannot undergo extreme changes over time [25, 26, 34]. Based on clinical data, the patient arterial wall area variation at 1 year was the only comparative data available in the calibration process. Mathematically, the objective and constraint functions were defined as follows:

$$f_A(\mathbf{x}) = |\Delta A_{ABM} - \Delta A_{patient}| \tag{3}$$

$$f_{ECM/cell}(\mathbf{x}) = \left. \frac{ECM/cell|_{1-year}}{ECM/cell|_{day\ 0}} \right|_{ABM} \tag{4}$$

where \mathbf{x} is the vector of the ABM parameters; $f_A(\mathbf{x})$ is the optimization objective, with ΔA_{ABM} and $\Delta A_{patient}$ being the cross-sectional variation of the wall area at 1 year predicted by the ABM and measured in the patient, respectively, and $f_{ECM/cell}(\mathbf{x})$ is the constraint, expressed in terms of the 1-year normalized ECM/SMC_{ratio_int} predicted by the ABM. The constrained optimization problem was written as:

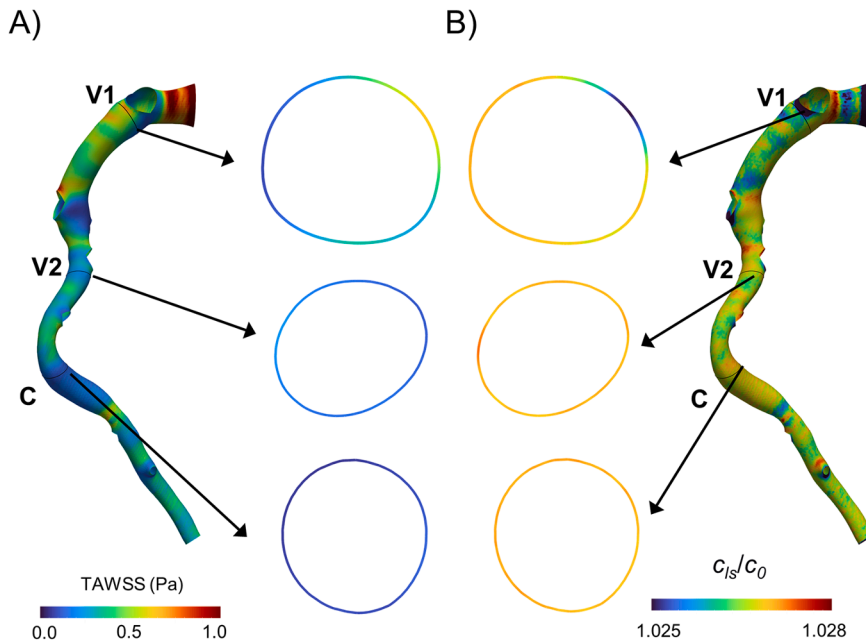


Fig. 2. A) Time-average wall shear stress (TAWSS) and B) normalized low-density-lipoprotein concentration at the lumen surface and at the three selected cross-sections (C, V1, V2). Side branches are not shown.

$$\begin{cases} \min & f_A(\mathbf{x}) \\ \mathbf{x} \in A & \\ \text{s.t.} : & \begin{cases} 0.5 < f_{ECM/cell}(\mathbf{x}) < 1.5 \\ A = \left\{ \mathbf{x} = [\alpha_2, \alpha_3, \alpha_7, \alpha_8] : \alpha_2 \in [0, 0.2], \alpha_3 \in [0, 0.7], \alpha_7 \in [0, 0.5], \right. \\ & \left. \alpha_8 \in [0, 0.5] \right\} \end{cases} \end{cases} \quad (5)$$

The range of the ABM parameters was defined by considering extreme case scenarios, ensuring that the event probabilities did not exceed 1 [25]. The non-dominated sorting genetic algorithm (NSGA-II) was adopted (in MATLAB environment) to find the optimal solution.

For the calibration process, cross-section C of the 3D coronary artery model was selected, while the other two cross-sections V1 and V2 were used for validation by running the ABM with the parameter values identified in the calibration process. Once calibrated and validated, the model was used to explore predictions under two scenarios: a long-term follow-up period (5 years) and an elevated LDL concentration (C0 = 5.2 mmol/L) up to 1-year follow-up [17].

The Mann–Whitney U-test was applied to compare the wall area variation (ΔA) between the model and the patient case, with statistical significance set for p-values < 0.05. The statistical analysis was performed in MATLAB environment.

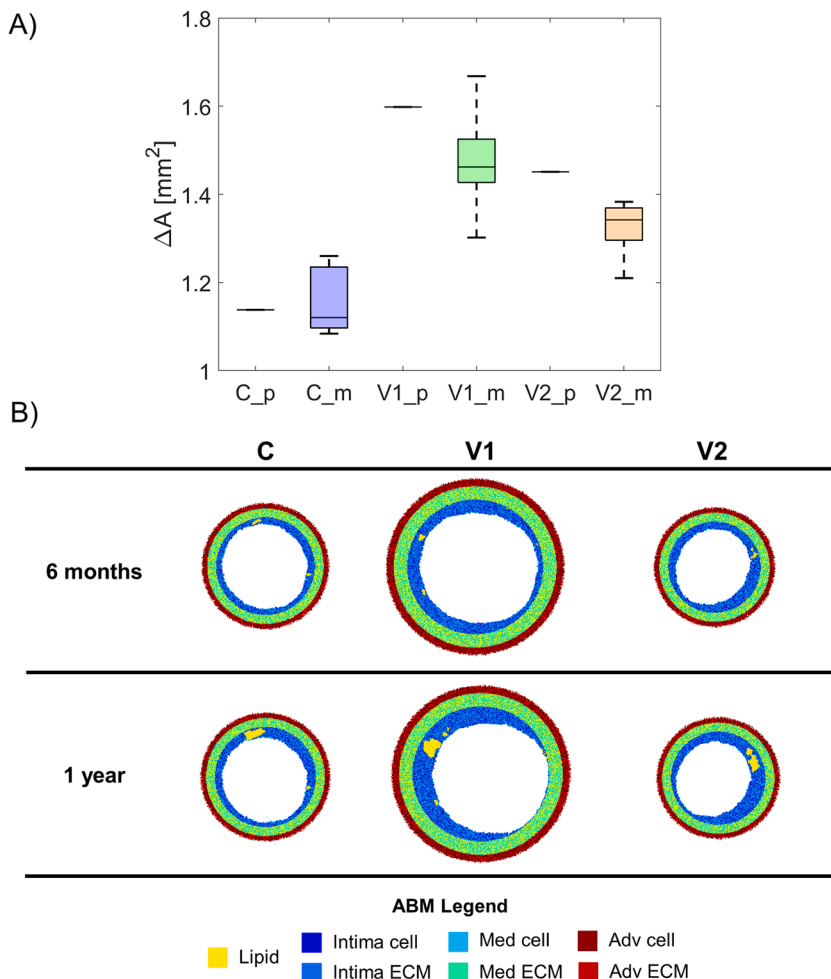


Fig. 3. A) 1-year arterial wall area variation (ΔA) in the three selected cross-sections (C, V1, V2) for the patient (p) and model (m) cases. As for the model case, results of ten simulations obtained by the calibrated agent-based model (ABM) are provided. B) ABM results at 6 months and at 1 year follow-up for the three selected cross-sections (C, V1, V2). For each cross-section, results were retrieved from one out of the ten ABM simulations, namely the one presenting the lumen configuration minimizing the root mean square deviation from the average one.

3. Results

3.1. Model calibration and validation

Fig. 2 shows the TAWSS distribution and the normalized LDL concentration at the lumen surface, used to initialize the ABM of plaque formation and progression.

The calibration procedure for cross-section C identified the optimal ABM parameters vector $\mathbf{x} = [\alpha_2 = 0.013, \alpha_3 = 0.1, \alpha_7 = 0.05, \alpha_8 = 0.05]$, which minimized the objective function while satisfying the constraint on $f_{ECM/cell}$, by performing 32 simulations. The ABM framework was then run using these optimal parameters. The goodness of the calibration was verified by performing ten simulations for cross-sections C, resulting in a 1.56% percentage difference between the ABM estimation and the real measurement for the 1-year ΔA . Similarly, ten simulations were run for cross-sections V1 and V2 to evaluate the model's ability to predict the ΔA at 1 year. The model successfully predicted the median patient-specific 1-year ΔA , with percentage difference of 8.52% and 7.52% between the ABM

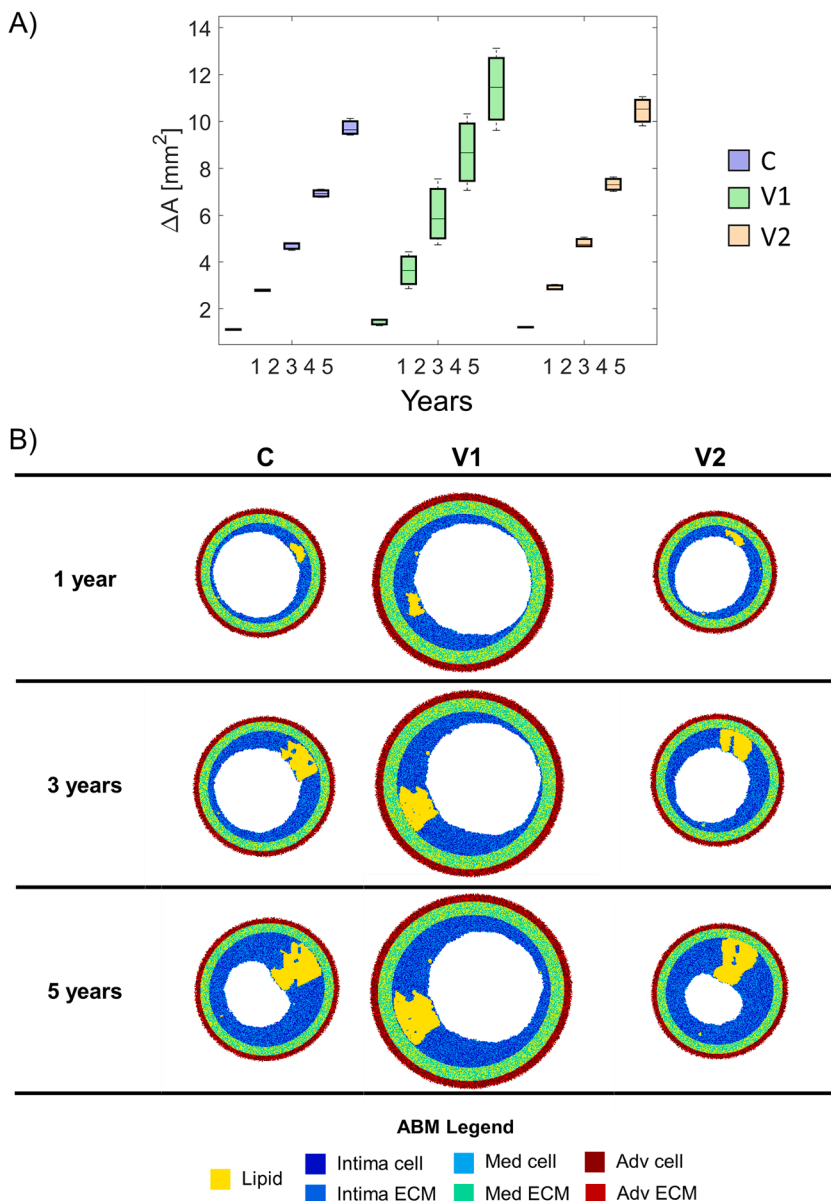


Fig. 4. A) Arterial wall area variation (ΔA) along 5 simulated years in the three selected cross-sections (C, V1, V2), obtained by ten simulations of the calibrated agent-based model (ABM). B) ABM results at 1, 3 and 5 years of follow-up for the three selected cross-sections (C, V1, V2). For each cross-section, results were retrieved from one out of the ten ABM simulations, namely the one presenting the lumen configuration minimizing the root mean square deviation from the average one.

estimations and the measurements, respectively. Fig. 3A presents the results of these simulations, showing the ΔA for cross-sections C, V1, and V2, along with comparisons to patient-specific data. Fig. 3B illustrates the ABM predictions at 6 months and 1 year of follow-up for each cross-section. In all three cross-sections, the increase in wall area led to outward expansion of the arterial wall without a reduction in lumen area (Glagov’s phenomenon). Indeed, the median $stenosis_{GL}$ levels at 1 year were 8%, 5%, and 9% for C, V1, and V2, respectively. Additionally, the ABM outputs showed asymmetric lipid plaque formation and intimal growth, localized in regions of low TAWSS and high LDL lumen polarization.

3.2. Long-term follow-up simulation

Over a 5-year follow-up, the calibrated ABM simulated a progressive increase in lipid content and intimal growth, resulting in a ΔA of 10-12 mm², compared to 1-1.5 mm² at 1 year (Fig. 4A). The remodeling process (Fig. 4B) exhibited outward arterial wall expansion up to year 3 in cross-sections C and V2, and up to year 5 for cross-section V1, which did not reach a $stenosis_{GL}$ of 30%. Cross-sections C and V2 exceeded this stenosis threshold at 3.5 years, reaching $stenosis_{GL}$ values of 50% and 54%, respectively, at 5 years. In contrast, cross-section V1 exhibited a $stenosis_{GL}$ of 31% at 5 years. Consistent with Glagov’s remodeling process, cross-sections C and V2 underwent lumen area reduction.

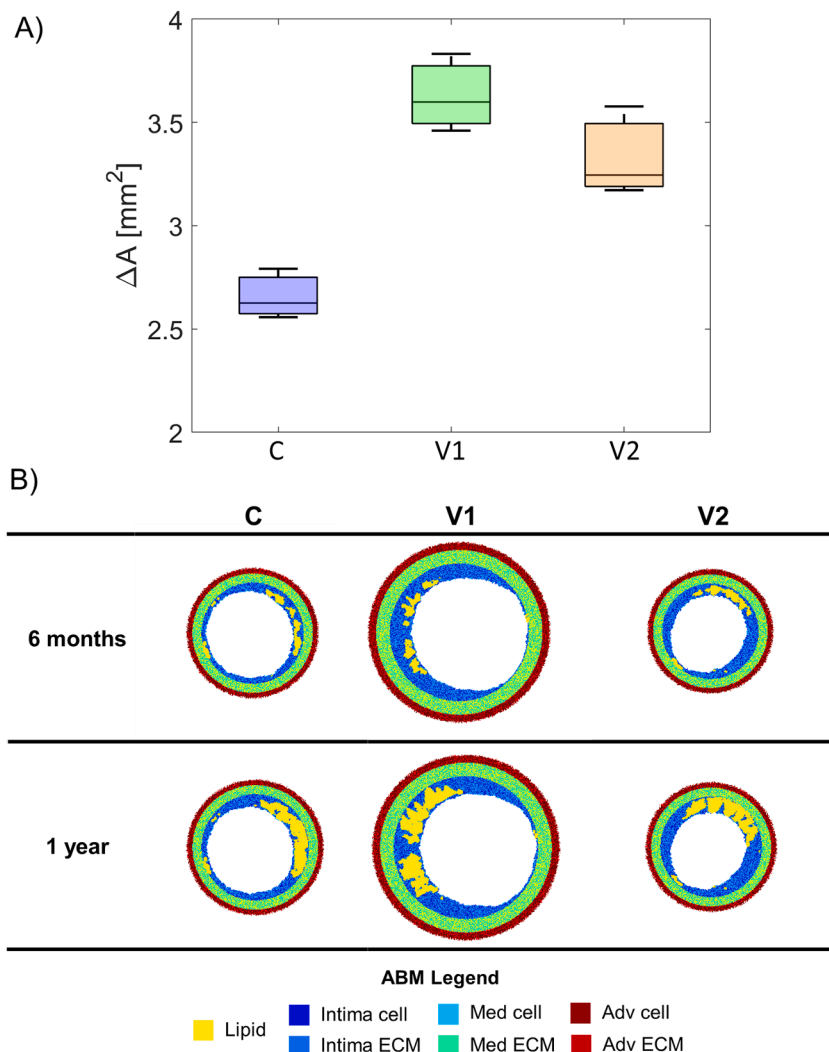


Fig. 5. A) 1-year arterial wall area variation (ΔA) in the three selected cross-sections (C, V1, V2), obtained by ten simulations of the calibrated agent-based model (ABM) in the high LDL scenario. B) ABM results at 6 months and 1 year of follow-up for the three selected cross-sections (C, V1, V2). For each cross-section, results were retrieved from one out of the ten ABM simulations, namely the one presenting the lumen configuration minimizing the root mean square deviation from the average one.

3.3. Impact of high LDL concentration on simulation outcomes

Under high blood LDL concentrations, the 1-year ΔA increased significantly ($p < 0.05$) (Fig. 5A). Specifically, cross-section C showed a median ΔA of 2.62 mm², V1 of 3.60 mm², and V2 of 3.24 mm² (vs. 1.12 mm², 1.46 mm², 1.24 mm², respectively, in the baseline case). Although the 1-year ΔA in the high LDL scenario was similar to the 2-year variation in the baseline case, the intimal lipid content differed markedly between the two scenarios, as emerges comparing Figs. 4 and 5. At 1 year, the absolute lipid content in the high LDL case matched the levels observed at 4 years in the baseline scenario. However, the percentage of lipids in the intimal area was substantially higher in the high LDL case, reaching 35% at 1 year, compared to 19% at 4 years in the baseline case (a percentage that remained stable at 5 years). Additionally, the spatial distribution of lipid content within the intima differed between the two scenarios. In the high LDL concentration case, lipid clusters were more diffusely distributed along the circumferential direction. This is likely due to the relationship between lipid influx and intimal growth rate, which promotes a circumferential lipid organization as a consequence of the limited intima thickness.

4. Discussion

The present study marks an advancement in the multiscale mechanobiological modeling of atherosclerosis, introducing an agent-based modeling framework for coronary plaque progression that incorporates a sophisticated description of LDL transport through the endothelium, replacing previous phenomenological assumptions with a mechanistic approach of higher biological fidelity. To the authors' knowledge, this is the first proof-of-concept application of such a framework in a patient-specific case, with initial validation.

Unlike previous agent-based modeling frameworks of atherosclerosis [24,40], which relied on simplified WSS-dependent probabilistic rules to estimate LDL infiltration, the present study adopts a physics-based approach that explicitly models both LDL transport in flowing blood and endothelial permeability. Specifically, LDL transport within the lumen is simulated through a mechanistic advection-diffusion model, while trans-endothelial flux is described through a three-pore model accounting for vesicular pathways, normal junctions, and leaky junctions. This integrated framework enables precise computation of LDL concentrations at the lumen surface and mechanistic estimation of LDL influx into the intima, thereby effectively bridging continuum-scale hemodynamics with ABM-driven arterial wall dynamics. While three-pore models have been widely employed to investigate trans-endothelial transport mechanisms [14], their integration into ABMs is relatively recent [23]. The strategy proposed in this study therefore represents a novel step toward multiscale, biologically faithful modeling of atherosclerosis. In addition, the present ABM incorporates biologically informed tissue remodeling dynamics. Notably, Glagov's phenomenon was included to capture compensatory outward remodeling phase that precedes lumen narrowing. Furthermore, a lipid-driven inflammatory input was introduced to represent the downstream inflammatory cascades influencing SMC and ECM behavior. Cellular dynamics were refined through the use of a WSS-dependent sigmoidal function calibrated on patient-specific data [25], thereby enhancing biological realism compared to the earlier ABM of atherosclerosis [24]. Overall, the present approach introduces substantial advancements over the previously developed framework [24], addressing key limitations such as the reliance on simplified lipid infiltration rules, the lack of compensatory remodeling mechanisms, and the absence of lipid-driven inflammatory signaling. The current hybrid framework integrates physics-based LDL transport, compensatory arterial remodeling, and inflammation-driven dynamics, yielding a more mechanistic and biologically grounded representation of disease progression. While these advancements come with an increased computational cost, they markedly enhance biological interpretability and predictive capability, making the model more suitable for hypothesis testing and potential translational applications.

Differently from the hybrid approach proposed here, fully-continuum modeling frameworks have been developed to integrate fluid dynamics, LDL transport in the lumen, through the endothelium and in the arterial wall, and plaque growth models [15,16,20,41]. These fully-continuum frameworks solve transport equations for LDL, inflammatory species, and SMCs while incorporating plaque growth models that depend on species accumulation, ultimately resulting in remodeled vessel geometries over time. Although the quantitative results (e.g., plaque growth extent and lumen narrowing) from fully-continuum and hybrid frameworks may be similar, outcomes such as spatial species distributions and morphological features differ significantly. The approach proposed here uniquely embeds the intrinsic randomness of biological systems and captures morphological details and tissue heterogeneity that are often missed by fully-continuum models, such as lipid core formation, irregular arterial wall and plaque shapes, and tissue heterogeneity.

The application of the present framework to a patient-specific coronary artery, along with its validation and explored use-case scenarios, underscores its potential as a platform for deciphering the mechanobiological pathways driving coronary plaque progression. Additionally, it offers a valuable tool for hypothesis generation and virtual population creation for *in-silico* trials (e.g., drug testing). The calibrated model predicted ΔA at 1 year in two patient-specific coronary cross-sections with an error of less than 10%. At 1 year, the remodeling process appeared characterized by small plaque formation and dominant outward remodeling, consistent with Glagov's phenomenon [3,4]. However, the 5-year simulation estimated potential patient-specific plaque evolution, suggesting increases in lipid core size and intimal thickness, ultimately leading to lumen area reduction due to sustained remodeling.

Additionally, the high blood LDL concentration scenario resulted in faster and more diffuse plaque growth. The model suggests that an increased LDL influx rate leads to a higher lipid-to-cell ratio in the intima, with an equivalent absolute lipid content, and promotes a more circumferential lipid distribution due to the intima's limited thickness. These findings should be validated through *in vitro* or *in vivo* experiments to confirm the predicted relationship between LDL influx, lipid organization, and intimal thickness. Such validation would further demonstrate the framework's value as a powerful hypothesis-generating tool. By providing predictions, the model can guide experimental designs and drive targeted investigations into the mechanisms of plaque development and lipid dynamics, bridging computational modeling with empirical research.

Despite its contributions, this study suffers from limitations. First, only one patient was considered to initially validate the proposed multiscale model. It must be noted that the present study focused on the development of a novel, complex and sophisticated methodology for modeling atherosclerotic plaque formation and progression. Thus, the patient-specific application served as a proof-of-concept aimed at demonstrating the potential applicability of the proposed solution to real-case scenarios. Future efforts will be devoted on the validation on more patient-specific cases. Second, only three cross-sections of a patient-specific coronary artery were analyzed using the ABM, as these were the only regions exhibiting a plaque growth over the 1-year follow-up. While this choice is consistent with the proof-of-concept nature of the study, future applications should, where data are available, incorporate a broader set of regions with arterial wall growth to more thoroughly assess the model's robustness. Additionally, to improve model generalizability and extend its applicability to vessel segments exhibiting wall thinning, future work should aim to investigate and integrate mechanobiological rules governing plaque regression, a phenomenon that is not currently captured, in the present framework. Third, validation was based solely on changes in arterial wall area. While this macroscopic validation implicitly supports the underlying mechanobiological rules, direct validation at the tissue composition or lipid content level would more robustly confirm the hypothesized cell-lipid dynamics and interactions driving plaque progression. With baseline and follow-up data detailing arterial wall composition (e.g., near-infrared spectroscopy), a multi-objective calibration could be conducted, including lipid content or plaque size alongside wall area variations. Nevertheless, it is important to emphasize that validating the model using the currently available patient-specific data, which include IVUS and CCTA imaging at multiple time points as well as blood velocity measurements, is itself a significant achievement, as such comprehensive longitudinal datasets are rare in clinical practice. Fourth, the three modules of the framework were coupled in a one-way fashion, with hemodynamic results from the CFD simulations serving as input to the ABM, while feedback effects of plaque growth on local hemodynamics were not considered. Although a two-way coupling framework has been previously developed and applied by our group for both atherosclerosis and restenosis applications [24–26,34], it was not implemented here for two main reasons: (i) within the 1-year follow-up considered for validation, Glagov's phenomenon led to outward remodeling without lumen narrowing, thereby minimizing hemodynamic alterations; and (ii) inward remodeling and associated lumen reduction were observed only in an exploratory long-term simulation (after ~3.5 years for sections C and V2), for which no patient data were available for comparison. In this context, incorporating two-way coupling would have significantly increased computational cost without altering the main findings or interpretation of the proof-of-concept scenario. Nevertheless, we acknowledge that iterative coupling could modestly affect the timing of long-term predictions, such as delaying plaque progression beyond 3.5 years, and represents a valuable improvement to pursue in future studies. Finally, plaque structural stress was not considered, despite its known association with compositional changes linked to vulnerability phenotypes [42]. Future work could integrate finite element analysis into the CFD-ABM framework, as done in [34]. This would enable the estimation of local plaque structural stress distributions and the exploration of its potential role in driving the mechanobiological rules within the ABM.

5. Conclusions

This study introduces a novel multiscale agent-based modeling framework for atherosclerosis, integrating LDL transport in the lumen through CFD simulations, a three-pore model of trans-endothelial LDL migration, and an ABM of lipid and cellular dynamics. The framework was applied to a patient-specific coronary artery and validated against follow-up data, significantly advancing the state of the art in modeling the mechanobiological pathways driving plaque growth. It provides valuable insights into LDL- and WSS-driven cellular dynamics in a patient-specific context. The simulated scenarios indicated that varying blood LDL concentrations can result in distinct plaque morphologies, ranging from concentrated to diffuse shapes. By enabling virtual experiments, the framework demonstrated its potential to accelerate scientific discovery by generating hypotheses that can guide or inform targeted *in vitro* or *in vivo* research.

Funding

Anna Corti is funded by the National Plan for NRRP Complementary Investments (PNC, established with the decree-law 6 May 2021, n. 59, converted by law n. 101 of 2021) in the call for the funding of research initiatives for technologies and innovative trajectories in the health and care sectors (Directorial Decree n. 931 of 06-06-2022) - project n. PNC0000003 - Advanced Technologies for Human-centred Medicine (project acronym: ANTHEM). This work reflects only the authors' views and opinions, neither the Ministry for University and Research nor the European Commission can be considered responsible for them.

CRedit authorship contribution statement

Anna Corti: Writing – review & editing, Writing – original draft, Visualization, Validation, Software, Project administration, Methodology, Investigation, Formal analysis, Conceptualization. **Giuseppe De Nisco:** Writing – review & editing, Methodology. **Jolanda J. Wentzel:** Writing – review & editing, Resources. **Francesco Migliavacca:** Writing – review & editing, Resources. **Umberto Morbiducci:** Writing – review & editing, Resources. **Claudio Chiastra:** Writing – review & editing, Supervision, Project administration, Conceptualization.

Declaration of competing interest

Anna Corti reports financial support was provided by National Plan for NRRP Complementary Investments. The other authors

declare that they have no known competing financial interests or personal relationships that could have appeared to influence the work reported in this paper.

Acknowledgements

The authors would like to thank Loris Barbiero, Alessia Budini and Tatiana Armillei (Politecnico di Milano, Milan, Italy) for their contribution to the work.

Supplementary materials

Supplementary material associated with this article can be found, in the online version, at [doi:10.1016/j.cma.2025.118427](https://doi.org/10.1016/j.cma.2025.118427).

Data availability

Data will be made available on request.

References

- [1] GBD 2021 Causes of Death Collaborators, Global burden of 288 causes of death and life expectancy decomposition in 204 countries and territories and 811 subnational locations, 1990–2021: a systematic analysis for the Global Burden of Disease Study 2021, *Lancet (Lond., Engl.)* 403 (2024) 2100–2132, [https://doi.org/10.1016/S0140-6736\(24\)00367-2](https://doi.org/10.1016/S0140-6736(24)00367-2).
- [2] J.F. Bentzon, F. Otsuka, R. Virmani, E. Falk, Mechanisms of Plaque Formation and Rupture, *Circ. Res.* 114 (2014) 1852–1866, <https://doi.org/10.1161/CIRCRESAHA.114.302721>.
- [3] S. Glagov, E. Weisenberg, C.K. Zarins, R. Stankunavicius, G.J. Kolettis, Compensatory enlargement of human atherosclerotic coronary arteries, *N. Engl. J. Med.* 316 (1987) 1371–1375, <https://doi.org/10.1056/NEJM198705283162204>.
- [4] Y. Birnbaum, M.C. Fishbein, H. Luo, T. Nishioka, R.J. Siegel, Regional remodeling of atherosclerotic arteries: a major determinant of clinical manifestations of disease, *J. Am. Coll. Cardiol.* 30 (1997) 1149–1164, [https://doi.org/10.1016/s0735-1097\(97\)00320-3](https://doi.org/10.1016/s0735-1097(97)00320-3).
- [5] P. Libby, J.E. Buring, L. Badimon, G.K. Hansson, J. Deanfield, M.S. Bittencourt, L. Tokgözoğlu, E.F. Lewis, Atherosclerosis, *Nat. Rev. Dis. Prim.* 5 (2019) 56, <https://doi.org/10.1038/s41572-019-0106-z>.
- [6] J. Borén, M.J. Chapman, R.M. Krauss, C.J. Packard, J.F. Bentzon, C.J. Binder, M.J. Daemen, L.L. Demer, R.A. Hegele, S.J. Nicholls, B.G. Nordestgaard, G. F. Watts, E. Bruckert, S. Fazio, B.A. Ference, I. Graham, J.D. Horton, U. Landmesser, U. Laufs, L. Masana, G. Pasterkamp, F.J. Raal, K.K. Ray, H. Schunkert, M.-R. Taskinen, B. van de Sluis, O. Wiklund, L. Tokgozoglu, A.L. Catapano, H.N. Ginsberg, Low-density lipoproteins cause atherosclerotic cardiovascular disease: pathophysiological, genetic, and therapeutic insights: a consensus statement from the European Atherosclerosis Society Consensus Panel, *Eur. Heart J.* 41 (2020) 2313–2330, <https://doi.org/10.1093/eurheartj/ehz962>.
- [7] B.R. Kwak, M. Bäck, M.-L. Bochaton-Piallat, G. Caligiuri, M.J.A.P. Daemen, P.F. Davies, I.E. Hoefer, P. Holvoet, H. Jo, R. Krams, S. Lehoux, C. Monaco, S. Steffens, R. Virmani, C. Weber, J.J. Wentzel, P.C. Evans, Biomechanical factors in atherosclerosis: mechanisms and clinical implications, *Eur. Heart J.* 35 (2014) 3013–3020, <https://doi.org/10.1093/eurheartj/ehu353>, 3020a–3020d.
- [8] Y.S. Chatzizisis, A.U. Coskun, M. Jonas, E.R. Edelman, C.L. Feldman, P.H. Stone, Role of endothelial shear stress in the natural history of coronary atherosclerosis and vascular remodeling: molecular, cellular, and vascular behavior, *J. Am. Coll. Cardiol.* 49 (2007) 2379–2393, <https://doi.org/10.1016/J.JACC.2007.02.059>.
- [9] C. Souilhol, M.C. Harmsen, P.C. Evans, G. Krenning, Endothelial-mesenchymal transition in atherosclerosis, *Cardiovasc. Res.* 114 (2018) 565–577, <https://doi.org/10.1093/cvr/cvx253>.
- [10] A.I. Sakellarios, C.V. Bourantas, S.L. Papadopoulou, Z. Tzirka, T. De Vries, P.H. Kitslaar, C. Girasis, K.K. Naka, D.I. Fotiadis, S. Veldhof, G.W. Stone, J.H. C. Reiber, L.K. Michalis, P.W. Serruys, P.J. De Feyter, H.M. Garcia-Garcia, Prediction of atherosclerotic disease progression using LDL transport modelling: A serial computed tomographic coronary angiographic study, *Eur. Heart J. Cardiovasc. Imaging* 18 (2017) 11–18, <https://doi.org/10.1093/ehjci/jew035>.
- [11] A.I. Sakellarios, P. Bizopoulos, M.I. Papafaklis, L. Athanasiou, T. Exarchos, C.V. Bourantas, K.K. Naka, A.J. Patterson, V.E.L. Young, J.H. Gillard, O. Parodi, L. K. Michalis, D.I. Fotiadis, Natural history of carotid atherosclerosis in relation to the hemodynamic environment: a low-density lipoprotein transport modeling study with serial magnetic resonance imaging in humans, *Angiology* 68 (2017) 109–118, <https://doi.org/10.1177/0003319716644138>.
- [12] V. Díaz-Zuccarini, G. Di Tomaso, O. Agu, C. Pichardo-Almarza, Towards personalised management of atherosclerosis via computational models in vascular clinics: Technology based on patient-specific simulation approach, *Healthc. Technol. Lett.* 1 (2014) 13–18, <https://doi.org/10.1049/hlt.2013.0040>.
- [13] G. De Nisco, P. Zhang, K. Calò, X. Liu, R. Ponzini, C. Bignardi, G. Rizzo, X. Deng, D. Gallo, U. Morbiducci, What is needed to make low-density lipoprotein transport in human aorta computational models suitable to explore links to atherosclerosis? Impact of initial and inflow boundary conditions, *J. Biomech.* 68 (2018) 33–42, <https://doi.org/10.1016/j.jbiomech.2017.12.009>.
- [14] A. Corti, M. Colombo, G. De Nisco, J.F. Rodriguez Matas, F. Migliavacca, C. Chiastra, Chapter 6 - computational investigation of the role of low-density lipoprotein and oxygen transport in atherosclerotic arteries, in: S. Becker, A.V. Kuznetsov, F. de Monte, G. Pontrelli, D. Zhao (Eds.), *Model. Mass Transp. Process. Biol. Media*, Academic Press, 2022, pp. 139–213, <https://doi.org/10.1016/B978-0-323-85740-6.00017-0>.
- [15] V. Calvez, J.G. Houot, N. Meunier, A. Raoult, G. Rusnakova, Mathematical and numerical modeling of early atherosclerotic lesions, *ESAIM Proc.* 30 (2010) 1–14, <https://doi.org/10.1051/proc/2010002>.
- [16] M.P. Thon, A. Hemmler, A. Glinzer, M. Mayr, M. Wildgruber, A. Zerneck-Madsen, M.W. Gee, A multiphysics approach for modeling early atherosclerosis, *Biomech. Model. Mechanobiol.* 17 (2018) 617–644, <https://doi.org/10.1007/s10237-017-0982-7>.
- [17] D.S. Pleouras, A.I. Sakellarios, P. Tsompou, V. Kigka, S. Kyriakidis, S. Rocchiccioli, D. Neglia, J. Knuuti, G. Pelosi, L.K. Michalis, D.I. Fotiadis, Simulation of atherosclerotic plaque growth using computational biomechanics and patient-specific data, *Sci. Rep.* 10 (2020) 17409, <https://doi.org/10.1038/s41598-020-74583-y>.
- [18] G. Di Tomaso, V. Daz-Zuccarini, C. Pichardo-Almarza, A multiscale model of atherosclerotic plaque formation at its early stage, *IEEE Trans. Biomed. Eng.* 58 (2011) 3460–3463, <https://doi.org/10.1109/TBME.2011.2165066>.
- [19] G. Di Tomaso, C. Pichardo-Almarza, O. Agu, V. Díaz-Zuccarini, A multiscale and Patient-specific computational framework of atherosclerosis formation and progression: A case study in the aorta and peripheral arteries, *Proced. Comput. Sci.* 51 (2015) 1118–1127, <https://doi.org/10.1016/j.procs.2015.05.281>.
- [20] M. Cilla, E. Peña, M.A. Martínez, Mathematical modelling of atheroma plaque formation and development in coronary arteries, *J. R. Soc. Interface.* 11 (2014) 20130866, <https://doi.org/10.1098/rsif.2013.0866>.
- [21] N. Filipovic, Z. Teng, M. Radovic, I. Saveljic, D. Fotiadis, O. Parodi, Computer simulation of three-dimensional plaque formation and progression in the carotid artery, *Med. Biol. Eng. Comput.* 51 (2013) 607–616, <https://doi.org/10.1007/s11517-012-1031-4>.

- [22] A. Corti, M. Colombo, F. Migliavacca, J.F. Rodriguez Matas, S. Casarin, C. Chiastra, Multiscale computational modeling of vascular adaptation: a systems biology approach using agent-based models, *Front. Bioeng. Biotechnol.* 9 (2021) 744560, <https://doi.org/10.3389/fbioe.2021.744560>.
- [23] R. Caballero, M.A. Martinez, E. Pena, Fully coupled hybrid in-silico modeling of atherosclerosis: a multi-scale approach integrating CFD, transport phenomena, and agent-based modeling, *Front. Bioeng. Biotechnol.* 13 (2025), <https://doi.org/10.3389/fbioe.2025.1549104>.
- [24] A. Corti, C. Chiastra, M. Colombo, M. Garbey, F. Migliavacca, S. Casarin, A fully coupled computational fluid dynamics – agent-based model of atherosclerotic plaque development: Multiscale modeling framework and parameter sensitivity analysis, *Comput. Biol. Med.* 118 (2020) 103623, <https://doi.org/10.1016/j.compbiomed.2020.103623>.
- [25] A. Corti, M. Colombo, J.M. Rozowsky, S. Casarin, Y. He, D. Carbonaro, F. Migliavacca, J.F. Rodriguez Matas, S.A. Berceci, C. Chiastra, A predictive multiscale model of in-stent restenosis in femoral arteries: linking haemodynamics and gene expression with an agent-based model of cellular dynamics, *J. R. Soc. Interface.* 19 (2022) 20210871, <https://doi.org/10.1098/rsif.2021.0871>.
- [26] A. Corti, F. Migliavacca, S.A. Berceci, C. Chiastra, Predicting 1-year in-stent restenosis in superficial femoral arteries through multiscale computational modelling, *J. R. Soc. Interface.* 20 (2023) 20220876, <https://doi.org/10.1098/rsif.2022.0876>.
- [27] V. Mazzi, G. De Nisco, K. Calò, C. Chiastra, J. Daemen, D.A. Steinman, J.J. Wentzel, U. Morbiducci, D. Gallo, Divergence of the normalized wall shear stress as an effective computational template of low-density lipoprotein polarization at the arterial blood-vessel wall interface, *Comput. Method. Program. Biomed.* 226 (2022) 107174, <https://doi.org/10.1016/j.cmpb.2022.107174>.
- [28] G. De Nisco, C. Chiastra, E.M.J. Hartman, A. Hoogendoorn, J. Daemen, K. Calò, D. Gallo, U. Morbiducci, J.J. Wentzel, Comparison of swine and human computational hemodynamics models for the study of coronary atherosclerosis, *Front. Bioeng. Biotechnol.* 9 (2021) 731924, <https://doi.org/10.3389/fbioe.2021.731924>.
- [29] E.M.J. Hartman, G. De Nisco, A.M. Kok, M. Tomaniak, F.M.A. Nous, S.-A. Korteland, F.J.H. Gijzen, W.K. den Dekker, R. Diletti, N.M.D.A. van Mieghem, J. M. Wilschut, F. Zijlstra, A.F.W. van der Steen, R.P.J. Budde, J. Daemen, J.J. Wentzel, Wall shear stress-related plaque growth of lipid-rich plaques in human coronary arteries: an near-infrared spectroscopy and optical coherence tomography study, *Cardiovasc. Res.* 119 (2023) 1021–1029, <https://doi.org/10.1093/cvr/cvac178>.
- [30] G. De Nisco, E.M.J. Hartman, E. Torta, J. Daemen, C. Chiastra, D. Gallo, U. Morbiducci, J.J. Wentzel, Predicting lipid-rich plaque progression in coronary arteries using multimodal imaging and wall shear stress signatures, *Arterioscler. Thromb. Vasc. Biol.* 44 (2024) 976–986, <https://doi.org/10.1161/ATVBAHA.123.320337>.
- [31] G. De Nisco, M. Lodi Rizzini, R. Verardi, C. Chiastra, A. Candreva, G. De Ferrari, F. D'Ascenzo, D. Gallo, U. Morbiducci, Modelling blood flow in coronary arteries: Newtonian or shear-thinning non-Newtonian rheology? *Comput. Method. Program. Biomed.* 242 (2023) 107823 <https://doi.org/10.1016/j.cmpb.2023.107823>.
- [32] U. Olgac, V. Kurtcuoglu, D. Poulidakos, Computational modeling of coupled blood-wall mass transport of LDL: effects of local wall shear stress, *Am. J. Physiol. - Hear. Circ. Physiol.* 294 (2008) 909–919, <https://doi.org/10.1152/ajpheart.01082.2007>.
- [33] U. Olgac, D. Poulidakos, S.C. Saur, H. Alkadhi, V. Kurtcuoglu, Patient-specific three-dimensional simulation of LDL accumulation in a human left coronary artery in its healthy and atherosclerotic states, *Am. J. Physiol. - Hear. Circ. Physiol.* 296 (2009), <https://doi.org/10.1152/ajpheart.01182.2008>.
- [34] A. Corti, M. Marradi, C. Çelikbudak Orhon, F. Boccafoschi, P. Büchler, J.F. Rodriguez Matas, C. Chiastra, Impact of tissue damage and hemodynamics on restenosis following percutaneous transluminal angioplasty: a patient-specific multiscale model, *Ann. Biomed. Eng.* 52 (2024) 2203–2220, <https://doi.org/10.1007/s10439-024-03520-1>.
- [35] A. Corti, A. McQueen, F. Migliavacca, C. Chiastra, S. McGinty, Investigating the effect of drug release on in-stent restenosis: a hybrid continuum - agent-based modelling approach, *Comput. Method. Program. Biomed.* 241 (2023) 107739, <https://doi.org/10.1016/j.cmpb.2023.107739>.
- [36] K.C. Koskinas, Y.S. Chatzizisis, A.P. Antoniadis, G.D. Giannoglou, Role of endothelial shear stress in stent restenosis and thrombosis: Pathophysiologic mechanisms and implications for clinical translation, *J. Am. Coll. Cardiol.* 59 (2012) 1337–1349, <https://doi.org/10.1016/j.jacc.2011.10.903>.
- [37] S. Mundi, M. Massaro, E. Scoditti, M.A. Carluccio, V.W.M. van Hinsbergh, M.L. Iruela-Arispe, R. De Caterina, Endothelial permeability, LDL deposition, and cardiovascular risk factors—a review, *Cardiovasc. Res.* 114 (2018) 35–52, <https://doi.org/10.1093/cvr/cvx226>.
- [38] A. Corti, M. Colombo, F. Migliavacca, S.A. Berceci, S. Casarin, J.F. Rodriguez Matas, C. Chiastra, Multiscale agent-based modeling of restenosis after percutaneous transluminal angioplasty: Effects of tissue damage and hemodynamics on cellular activity, *Comput. Biol. Med.* 147 (2022) 105753, <https://doi.org/10.1016/j.compbiomed.2022.105753>.
- [39] P.-W. Fok, Multi-layer mechanical model of Glagov remodeling in coronary arteries: Differences between in-vivo and ex-vivo measurements, *PLoS One* 11 (2016) e0159304, <https://doi.org/10.1371/journal.pone.0159304>.
- [40] R. Bhui, H.N. Hayenga, An agent-based model of leukocyte transendothelial migration during atherogenesis, *PLoS Comput. Biol.* 13 (2017) 1–23, <https://doi.org/10.1371/journal.pcbi.1005523>.
- [41] N. Filipovic, D. Nikolic, I. Saveljic, Z. Milosevic, T. Exarchos, G. Pelosi, O. Parodi, Computer simulation of three-dimensional plaque formation and progression in the coronary artery, *Comput. Fluid.* 88 (2013) 826–833, <https://doi.org/10.1016/j.compfluid.2013.07.006>.
- [42] C. Costopoulos, L.H. Timmins, Y. Huang, O.Y. Hung, D.S. Molony, A.J. Brown, E.L. Davis, Z. Teng, J.H. Gillard, H. Samady, M.R. Bennett, Impact of combined plaque structural stress and wall shear stress on coronary plaque progression, regression, and changes in composition, *Eur. Heart J.* 40 (2019) 1411–1422, <https://doi.org/10.1093/eurheartj/ehz132>.